Expansion-induced Three-part Morphology of the 2021 December 4 Coronal Mass Ejection

Liping Yang[1] , Xueshang Feng[1] , Fang Shen[1,2] , Ming Xiong[1,2] , Chenglong Shen[3,4] , Yutian Chi[5] , Yuming Wang[3,4] , Kuo Yan[6], Mengxuan Ma[1,2], Yufen Zhou[1], Man Zhang[1] , and Xinhua Zhao[1]

[1] SIGMA Weather Group, State Key Laboratory for Space Weather, National Space Science Center, Chinese Academy of Sciences, Beijing 100190, People's Republic of China; lpyang@swl.ac.cn, fengx@swl.ac.cn
[2] College of Earth and Planetary Sciences, University of Chinese Academy of Sciences, Beijing 100049, People's Republic of China
[3] Deep Space Exploration Laboratory/School of Earth and Space Sciences, University of Science and Technology of China, Hefei 230026, People's Republic of China
[4] CAS Center for Excellence in Comparative Planetology, University of Science and Technology of China, Hefei 230026, People's Republic of China
[5] Institute of Deep Space Sciences, Deep Space Exploration Laboratory, Hefei 230026, People's Republic of China
[6] Shenzhen Key Laboratory of Numerical Prediction for Space Storm, School of Aerospace, Harbin Institute of Technology, Shenzhen 518055, People's Republic of China

Abstract

The typical structure of a coronal mass ejection (CME) was identified as a three-part morphology, which includes a bright front, a dark cavity, and a bright core, with the cavity and the core generally regarded as flux rope and eruptive prominence. However, there are three-part CMEs that are not associated with prominences. In this work, we conduct a high-resolution simulation of the 2021 December 4 CME mimicked with a spheromak flux rope to investigate the formation of the three-part morphology in the solar corona. The CME, with no signatures of prominence at the beginning, evolves into a high–low–high-density structure, which appears in a coronagraph image as a bright front immediately followed by a dark cavity with a bright core behind. The moving and expanding spheromak flux rope sweeps up the solar wind plasma and meanwhile, the plasma at its utmost edge is compressed, which produces the high-density front overlying the flux rope. It is also found that the expansion of the flux rope is uneven, with strong expansion at its outlying area and weak expansion at its central and rear parts. The differential expansion rates lead to the distinct rarefaction rates of the plasma, which results in the formation of the low-density cavity and the high-density core within the flux rope. Our three-dimensional study for the first time demonstrates that the evolution of the flux rope can self-consistently generate the three-part density structure, which improves the understanding of CME's morphologies in coronagraph images.

Unified Astronomy Thesaurus concepts: Solar coronal mass ejections (310); Solar wind (1534); Magnetohydrodynamics (1964)

Materials only available in the online version of record: animations

1. Introduction

Coronal mass ejections (CMEs) are the energetic eruptions of the large-scale, coherent magnetic plasma with the temperature of the solar corona. A typical CME has a width of $\sim45°$, a mass of $\sim10^{15}$ g, an energy of $\sim10^{30}$ erg, a speed of $\sim500\,\mathrm{km\,s^{-1}}$, and a magnetic flux rope-like structure (W. Manchester et al. 2017; J. Zhang et al. 2021). CMEs usually leave off the Sun and enter into the interplanetary space. When CMEs' interplanetary manifestations (ICMEs) are directed at the Earth and planets, they can be responsible for auroras, geomagnetic storms, and solar energetic particles, and change the plasma environments of planets, such as Venus and Mars (X. Feng et al. 2013; C. Shen et al. 2017; N. Gopalswamy 2022).

Since the 1970s, the knowledge of CME has been learned from spaceborne coronagraph experiments on Seventh Orbiting Solar Observatory (1971–1973), Skylab (1973–1974), Solwind (1979–1985), Solar Maximum Mission (1980, 1984–1989), Solar and Heliospheric Observatory (SOHO; 1995–), Solar Terrestrial Relations Observatory (STEREO; 2006–), Parker

Solar Probe (2018–), Solar Orbiter (2020–), and so on (R. A. Howard et al. 2023). From their appearance of a bright white-light feature in the coronagraph field of view, it is found that CMEs occur at the Sun with varying morphologies, sizes, and velocities. Particular morphological structures of CMEs in the white-light coronagraph contain three-part CMEs where the bright front is immediately followed by a darker cavity frequently with an embedded bright core (R. H. Munro et al. 1979; R. M. E. Illing & A. J. Hundhausen 1985), loop CMEs that have just a bright loop front (R. A. Howard et al. 1985; A. Vourlidas et al. 2013), and halo CMEs with their quasi-circular appearance (R. A. Howard et al. 1982). According to the angular width in the sky plane, CMEs are also classified into narrow CMEs that show jet-like motions and normal CMEs that feature a closed frontal loop (P. F. Chen 2011). Measured projected speeds of CMEs range from a few kilometers per second (near the Sun) to $>2000\,\mathrm{km\,s^{-1}}$, occasionally reaching $3500\,\mathrm{km\,s^{-1}}$ (S. Yashiro et al. 2004).

The three-part morphology has become a typical type of CME structure even though only about one-third of the events could be identified to possess all three parts (R. H. Munro et al. 1979; D. F. Webb & A. J. Hundhausen 1987). As coronagraphs record photospheric light scattered by electrons in the corona, the three-part structure actually reflects a high–low–high-

density structure of CMEs. The bright core in the white-light images has an almost identical location to the erupting prominence in Hα images, which suggests that the dense core material comes from the pre-eruption prominence (E. Hildner et al. 1975; N. Gopalswamy et al. 2006). It is theoretically and observationally recognized that CMEs can be driven by the eruption of magnetic flux ropes with a helical magnetic field wrapping around their central axial field lines (B. C. Low 1994; J. Chen et al. 1997; B. E. Wood & R. A. Howard 2009; X. Cheng et al. 2011; A. Vourlidas et al. 2013; C. Jiang et al. 2021; L. Li et al. 2024). The Large Angle and Spectrometric Coronagraph (LASCO) images enable the opportunity for a detailed comparison between observations and theoretical predictions of flux rope structures, which permits a linkage of the low-density cavity with the hollow flux rope structure (K. P. Dere et al. 1999; S. E. Gibson et al. 2006; S. Patsourakos et al. 2010). Tracking of the cavities to 1 au confirms that a cavity passes over a spacecraft as a rotation of the magnetic vector that can be fitted by a magnetic flux rope (C. Möstl et al. 2009; A. P. Rouillard et al. 2009). Meanwhile, the propagation and expansion of an erupted flux rope sweep up materials at its front, which hints that the brightness of the CMEs' front originates from a compression of the ambient plasma (X. Cheng et al. 2012; A. Vourlidas et al. 2013). The cool prominence can suspend in the dips of flux ropes as a result of the balance between gravity and magnetic tension force, which demonstrates that the system of ejected flux ropes accounts for well the observed three-part morphology of CMEs (A. F. R. Thernisien et al. 2006).

However, this perspective is challenged by the following facts. After searching for in situ prominence signatures with large abundances of low-temperature plasma at the trailing portion of ICMEs, it is found that prominence materials are rarely detected at far distances from the Sun (R. Schwenn et al. 1980; S. Yao et al. 2010; B. E. Wood et al. 2016). There are also some observations near the Sun displaying that some three-part CMEs do not correlate to eruptive prominences, which points out that the bright core of the three-part CMEs could be brought about by the natural evolution of a flux rope without dense prominence materials (T. A. Howard et al. 2017; H. Q. Song et al. 2017, 2019; A. M. Veronig et al. 2018; B. T. Wang et al. 2022). H. Song et al. (2023b) reported a CME event on 2014 June 14 showing that the CME core matches with a hot-channel flux rope and the CME front corresponds to the plasma pileup along magnetic arcades as recorded seamlessly by multiple space- and ground-based instruments. To explain the three-part CMEs without signatures of prominences, a new view suggests that a flux rope represents the bright core, the plasma pileup along coronal loops overlying the flux rope results in the bright front, and the low-density zone between the flux rope and the coronal loops is observed as the dark cavity (H. Q. Song et al. 2017, 2019; H. Song et al. 2022, 2023b, 2023a).

Numerical simulations have been conducted to understand the morphology of CMEs. By superimposing the three-dimensional (3D) Gibson–Low flux rope inside the coronal streamer belt created by the interaction between a dipole field and heated plasma, W. B. Manchester et al. (2004) numerically studied the propagation of a CME in the bimodal solar wind, and synthesized white-light coronagraph images of the modeled CME, which showed features of plasma pileup ahead of the erupting flux rope and depletion of density behind the

expanding flux rope. P. Riley et al. (2008) conducted a 2.5-dimensional simulation of magnetic flux cancellation near the neutral line of a streamer belt to investigate the relationship between the three-part structure observed by coronagraph and ICME signatures measured in interplanetary space. In their simulation, the dark cavity is closely associated with the flux rope driven by the flux cancellation, the bright core origins from prominence materials forming at the center of the flux rope, and the bright front is composed of the streamer belt, rather than a result of the ambient plasma pileup in front of the flux rope. Using the Gibson–Low flux rope model with support of dense prominence plasma, M. Jin et al. (2017a) simulated a CME event on the background solar wind starting from the upper chromosphere. Their simulation successfully captured the three-part density structure of the CME. Z. X. Mei et al. (2020) and Z. Mei et al. (2023) modeled the early eruption of a Titov–Démoulin flux rope with prominence materials and its subsequent propagation in the near-Sun region. They found that a helical current boundary appeared as a bright front feature in the synthetic white-light images.

Due to the complexity of the CME appearance and dynamics, it is still unclear how a CME without signatures of prominence develops a three-part morphology. In this work, we investigate the natural evolution of a spheromak flux rope under a high-resolution simulation of the 2021 December 4 CME (Y. Chi et al. 2023a, 2023b). At the initial time, the CME possesses a uniform distribution of density, and with time passing by, the CME displays a high–low–high-density structure, which approaches the three-part morphology of CMEs in white-light coronagraph images. The paper is organized as follows: in Section 2, we briefly describe our modeling setup, and in Section 3, we present simulation results and the corresponding analyses. Section 4 is reserved for summary and discussion.

2. Modeling Setup

We simulate the 2021 December 4 CME in the solar corona using the 3D adaptive mesh refinement (AMR) solar-interplanetary spacetime (SIP) conservation element and solution element (CESE) magnetohydrodynamics solar wind model (X. Feng et al. 2010, 2012; L. Yang et al. 2021, 2023). The simulation settings necessary for this event are specified in M. Ma et al. (2024). Here, we give some details. We first obtain the ambient solar wind in which the CME propagates. The coupling among Parker's hydrodynamic isothermal solution (E. N. Parker 1963), a potential field based on the Global Oscillation Network Group magnetogram of Carrington rotation 2251, and a volumetric heating (L. P. Yang et al. 2012) helps to achieve a quasi-steady, realistic solution of the solar wind, which shows the high-density streamers with the low-speed plasma and the polar open fields where the high-speed wind lies.

To describe the flux rope structure of the 2021 December 4 CME, a spheromak CME (R. Kataoka et al. 2009; Y. Zhou et al. 2014; M. Zhang et al. 2019; L. Yang et al. 2021; G. J. Koehn et al. 2022; E. Palmerio et al. 2023; C. Scolini & E. Palmerio 2024) is superposed onto the simulated solar wind. The initial parameters of the spheromak CME are confined by white-light coronagraph observations (M. Ma et al. 2024). To avoid the matter that the dense core of prominence materials is beforehand placed into the flux rope, the initial distribution of density in the spheromak CME is set to be uniform. A passive
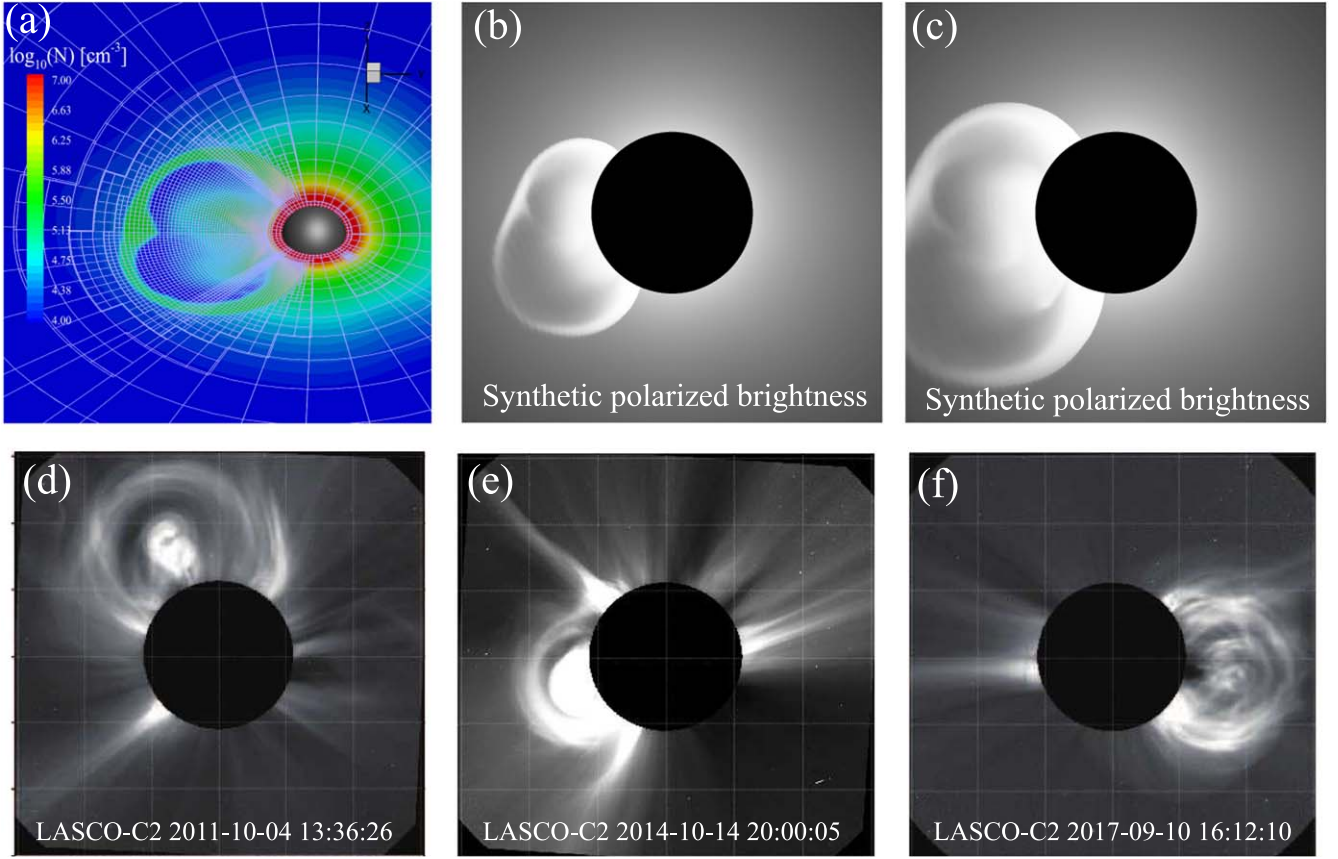
Figure 1. Simulated distribution of the number density N on the y–z and x–y planes (a), synthetic LASCO-C2 images of the white-light intensity as viewed from the x-axis at $t = 0.22$ hr (b) and $t = 0.43$ hr (c), as well as three-part CMEs as appeared in LASCO-C2 on 2011 October 4 (d), 2014 October 14 (e), and 2017 September 10 (f). In panel (a), the black sphere marks the Sun, and the white quadrilaterals denote the grid blocks, which are divided into $6 \times 6 \times 6$ grids. Panels (a) and (b) are accompanied by animations that present the evolution processes of the number density and synthetic white-light intensity from $t = 0.00$ to $t = 1.57$ hr with a duration of 0.03 hr.

(An animation of this figure is available in the online article.)

tracer with a value greater than 0 ($\rho_c > 0$) is used here to tag the CME (L. Yang et al. 2023). The passive tracer is advected by the flow according to its own continuity equation and traces the trajectory of the tagged plasma. The passive tracer starts with nonnegative values in the entire domain, it will keep being nonnegative.

To achieve the high resolution in the CME as well as its driven shock, we implement the AMR technique and design the thresholds of the refining and coarsening grid. During the calculation, we apply the highest resolution at any location with $\rho_c > 0$ or $(\nabla \cdot \boldsymbol{u}/(|\boldsymbol{u}| + \epsilon * c_s))^2 > \kappa\tau$, where $\boldsymbol{u}$ is velocity, $\epsilon = 1 \times 10^{-5}$, c_s is sonic speed, τ is the average value of $(\nabla \cdot \boldsymbol{u}/(|\boldsymbol{u}| + \epsilon * c_s))^2$ in the full domain, and κ is delicately tuned to be about 20. The criterion with ρ_c is to capture the CME body, and the criterion with the velocity aims to resolve the locations with large compression, e.g., shock front with piled-up plasma. With these settings, six levels of grid refinement are achieved to resolve the CME and the shock under the global modeling of the solar wind. The actual resolution used is $\delta r \approx \delta\theta \approx \delta\phi \approx 0.005\, Rs$ at about $5\, Rs$, where Rs is the solar radius, and $\delta r, \delta\theta$, and $\delta\phi$ are the grid sizes in the radial, latitude, and longitude directions, respectively. The time when the spheromak CME is initialized is set as $t = 0$ hr.

As shown in M. Ma et al. (2024), the position and overall shape of the simulated CME in the solar corona are comparable to those observed by SOHO/LASCO and STEREO-A/COR2. The features of the simulated CME in the interplanetary space

generally conform to those measured by the BepiColombo and the MAVEN/Tianwen-1. The 2021 December 4 CME is ejected from the backside of the Sun relative to observers and is thus imaged as a partial halo CME in the white-light image (Y. Chi et al. 2023b). To cover this shortage, here, we synthesize white-light radiance patterns of the CME viewed from different perspectives from the simulated 3D distribution of density, using a specific forward-modeling procedure of Thomson-scattering white light (M. Xiong et al. 2013).

3. Results

Figure 1(a) showcases the distribution of the number density N on the y–z and x–y planes. It is easily found that the modeled CME has a high–low–high-density structure. At the utmost edge of the CME, the number density is $\sim 10^{5.5}\,\mathrm{cm}^{-3}$, which is about 10 times the number density at the CME middle part shown as the blue color in Figure 1(a). At the central part of the CME, the number density increases to $\sim 10^6\,\mathrm{cm}^{-3}$. It is worth mentioning that P. F. Wyper et al. (2024) initiated the CME without any density structures in an ideal isothermal gravitationally stratified atmosphere, and the resulting CME also displays a dense core. Besides displaying two-dimensional (2D) representations of the number density on various planes, we present the density as it can be viewed in a coronagraph image. Figure 1(b) shows synthetic Thompson-scattered white-light brightness as viewed from the x-axis. The

synthesized coronagraph image clearly reveals that the modeled CME holds the three-part morphology, which is a bright front immediately followed by a dark cavity with an embedded bright core.

The bright core presented herein differs from that in the typical three-part morphology of CMEs (Figure 1(d), in which the core is substantially brighter than the front. In this study, the brightness of the core is comparable to that of the front, similar to the three-part structure of the CME on 2017 September 10, (Figure 1(f)). A side-by-side comparison between the simulated images and the observed ones also indicates that, in contrast to the CME cores on 2011 October 4, (Figure 1(d)) and on 2017 September 10, (Figure 1(f)), the simulated core does not conspicuously suspend above the solar surface, a characteristic similar to that of the CME core on 2014 October 14 (Figure 1(e)). This phenomenon could potentially be ascribed to the fact that the CME remains in close proximity to the Sun at this time moment, and the used spheromak flux rope fails to uphold the global features of CMEs that the foot points of flux ropes keep anchored to the Sun.

It is instructive to investigate the evolution of the CME's number density and the CME's white-light signatures, which are shown in the animations of Figure 1. It can be seen that the bright, high-density front first appears, and then it is the dark, low-density cavity. At last, the bright, high-density core is readily discerned. As the CME moves out, the CME front widens considerably. Meanwhile, the volume of the CME cavity becomes large, and its density drops evidently. The plasma rarefaction in the CME cavity seems associated with the growth of the CME volume. With the CME cavity extending into the CME legs, the CME core is separated from the CME front and becomes isolated, which indicates that the CME develops into a three-part morphology.

In Figure 1, the animations show something like a "collapse" of the lower coronal density and downward extension of the cavity in the early stage of the CME evolution that forms the bright core part, which seems different from typical best observations that the CME core propagates with the CME in white-light coronagraphs (A. Vourlidas et al. 2013; H. Q. Song et al. 2017). In the current study, we do not focus on the eruption of the CME in the inner corona ($1\text{--}1.5\,Rs$), but instead, we position the spheromak flux rope in the middle corona ($1.5\text{--}3\,Rs$) to monitor the CME evolution in the outer corona ($>3\,Rs$). Consequently, the synthetic white-light images present the formation process of the CME's three-part configuration. It remains uncertain where the three-part configuration of CMEs originates. The animations of Figure 1, along with Figures 1(b) and (c) distinctly reveal that after its formation, the core moves outward, albeit for a brief duration. Subsequently, the core progressively diminishes in size and eventually fades away.

Figures 2(a) and (b) display the side and back view of the CME flux rope structure as well as the distribution of the number density therein, which demonstrates the counterparts of the CME's three-part appearance. The dense front overlies the flux rope, which is identified from the rotation of the magnetic field lines. In combination with Figures 2(a) and (b) with the accompanying animations of Figure 1, it is apparent that the dense front is due to the pileup of materials as the flux rope propagates through the solar wind. The narrow width of the front indicates that the pileup occurs over a sharp boundary (A. Vourlidas et al. 2013). Figures 2(a) and (b) further show that both the tenuous cavity and the dense core are situated within

the flux rope, with the cavity being at the outlying area of the flux rope and the core at the central and rear parts of the flux rope.

We extract the CME's parameters along two lines, which pass through the flank (Line 1 in Figure 2(a) and center (Line 2 in Figure 2(b)) of the flux rope. Figures 2(c) and (d) show the variations of the CME's parameters along Line 1 and Line 2, respectively, from which it is illustrated again that the high-density front is at the utmost boundary of the CME and both the low-density cavity and the high-density core originate from the CME flux rope structure. In Figures 2(c) and (d), the flux rope is featured by the nonzero tracer ρ_c, the strong magnetic field strength B_{tot}, the large radial speed V_r, the very low plasma $\beta(=P_{\text{th}}/P_{\text{mag}}$, P_{th} is the thermal pressure and P_{mag} is the magnetic pressure.), and the low temperature T. For Line 1, which is connected to the Sun, we use the CME tracer $\rho_c > 0.01$ to identify the utmost boundary of the CME and a discontinuity to discern the inner boundary of the CME. For Line 2, which is detached from the Sun, the condition of $\rho_c > 0.01$ is enough to recognize the CME from the solar wind. The shaded areas in Figures 2(c) and (d) indicate the intervals of the CME, from which one thing to note is that there is no evident border between the cavity, which is concentrated around the minimums of the number density, and the core, which is near the maximum of the number density in Figure 2(d). The other thing to note is that the materials of the high-density and high-temperature front, which centers the utmost boundaries of the CME, consist of not only the pileup solar wind plasma with $\rho_c = 0.00$ but also the squeezed CME plasma, which is at the utmost edge of the CME.

The accompanying animations of Figures 2(a) and (b) showcase that the formation of the low-density cavity seems related to the expansion of the flux rope. As the flux rope transports outward, its volume quickly becomes large. Since the outlying area of the flux rope inflates first and quickly, the magnetic field lines at the outlying area of the flux rope tend to spread out over the greater region than those at the central part of the flux rope. This implies that the density at the outlying area of the flux rope dilutes more quickly than at the central part of the flux rope, and thus the cavity appears.

To clearly state that the generation of the low-density cavity within the flux rope is due to the strong expansion at the outer layer of the flux rope, Figure 3 plots the 3D distribution of the expansion speed V_{exp} and the Lorentz force F_{Lorentz} within the flux rope, with the arrows marking their directions. We calculate V_{exp} and F_{Lorentz} as follows. The CME's expansion velocity V_{exp} and propagation velocity V_{pro} contribute to its total velocity $\boldsymbol{u}$. Separating the expansion and propagation velocities from the total velocity is nontrivial (R. Schwenn et al. 2005; N. Gopalswamy et al. 2012; C. Scolini et al. 2019). Here, we compute the propagation velocity of the CME as the average velocity of the CME, that is, $V_{\text{pro}} = \text{mean}(\boldsymbol{u}(\rho_c > 0.01))$, with the CME being tagged by the tracer $\rho_c > 0.01$. The expansion velocity of the CME is directly quantified by $V_{\text{exp}} = \boldsymbol{u} - V_{\text{pro}}$. The Lorentz force acting on the CME is $F_{\text{Lorentz}} = \boldsymbol{j} \times \boldsymbol{B} = (\boldsymbol{B} \cdot \nabla)\boldsymbol{B} - \nabla B_{\text{tot}}/2$, where $\boldsymbol{B}$ is the magnetic field and $\boldsymbol{j} = \nabla \times \boldsymbol{B}$ is the current density. The Lorentz force is composed of the tension force $(\boldsymbol{B} \cdot \nabla)\boldsymbol{B}$ and the magnetic pressure gradient $-\nabla B_{\text{tot}}/2$, the imbalance between which leads to the expansion of the CME.

Figure 3(a) displays that the flux rope bulges at different rates. The direction of the expansion is almost perpendicular to the CME surface of $\rho_c = 0.01$ and points away from the center of the
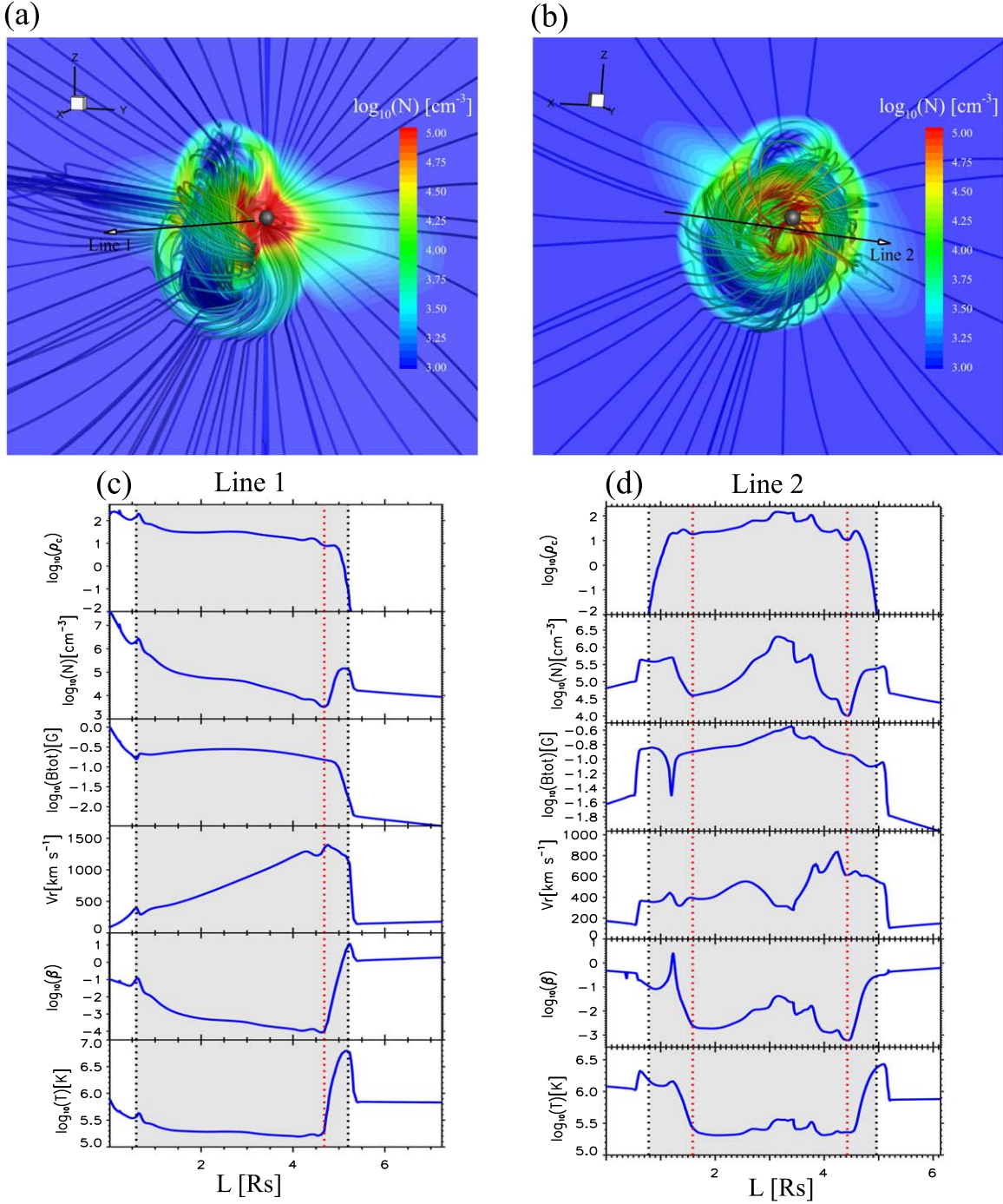
Figure 2. Panels (a) and (b) show the side (a) and back (b) view of the CME flux rope structure at $t = 0.52$ hr. The colored planes mark the y–z (a) and x–z (b) planes and the colored solid lines denote magnetic field lines, with the colors representing the values of the number density N. The black sphere marks the Sun. The accompanying animations of panels (a) and (b) are available. Panel (c) and (d) show the variations of the tracer ρ_c, the number density N, the magnetic field strength $B_{\rm tot}$, the radial speed V_r, the plasma β, and the temperature T along Line 1 (black line with an arrow in panel (a)) and Line 2 (black line with an arrow in panel (b)), respectively. The shaded areas indicate the intervals of the CME, and the dashed red line marks the minimums of the number density N. Panels (a) and (b) are accompanied by animations that present the evolution process of the CME flux rope structure from $t = 0.00$ to $t = 1.05$ hr with a duration of 0.03 hr.

(An animation of this figure is available in the online article.)

CME. The expansion speed at the outlying area of the flux rope is $\sim 1000\,{\rm km\,s^{-1}}$, which is far higher than the expansion speed of $\sim 500\,{\rm km\,s^{-1}}$ at the central and rear parts of the flux rope. As the plasma is frozen with the magnetic fields, the different expansion rates mean the district rarefaction rates of the plasma, which supports that the low-density cavity and the high-density core can form at the different parts of the flux rope. The distribution of the Lorentz force acting on the CME in

Figure 3(b) helps to understand the different expansion velocities at the different parts of the flux rope. The Lorentz force at the outlying area of the flux rope is stronger than at the central part of the flux rope, and its direction points outward predominantly along the normal of the CME surface. This explains why the strong expansion takes place at the outlying area of the flux rope.

Figure 4 presents the distributions of the expansion speed $V_{\rm exp}$, the number density N, and the temperature T at the
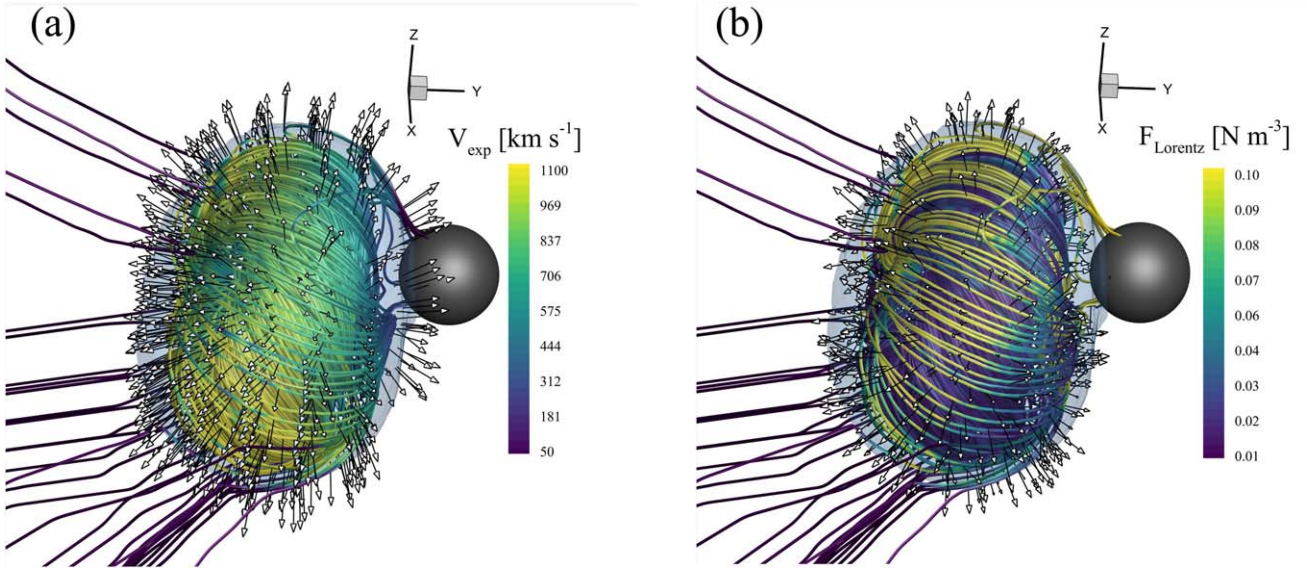
Figure 3. 3D distributions of the expansion speed (panel (a)) and the Lorentz force (panel (b)) within the flux rope structure of the modeled CME at $t = 0.43$ hr. The colored solid lines denote magnetic field lines, with the colors showing the magnitudes of the expansion velocity V_{exp} and the Lorentz force $F_{Lorentz}$. The arrows indicate the directions of $\boldsymbol{V}_{exp}$ and $\boldsymbol{F}_{Lorentz}$. The gray transparent 3D surface marks the contour of the $\rho_c = 0.01$ surface, and the black sphere represents the Sun.
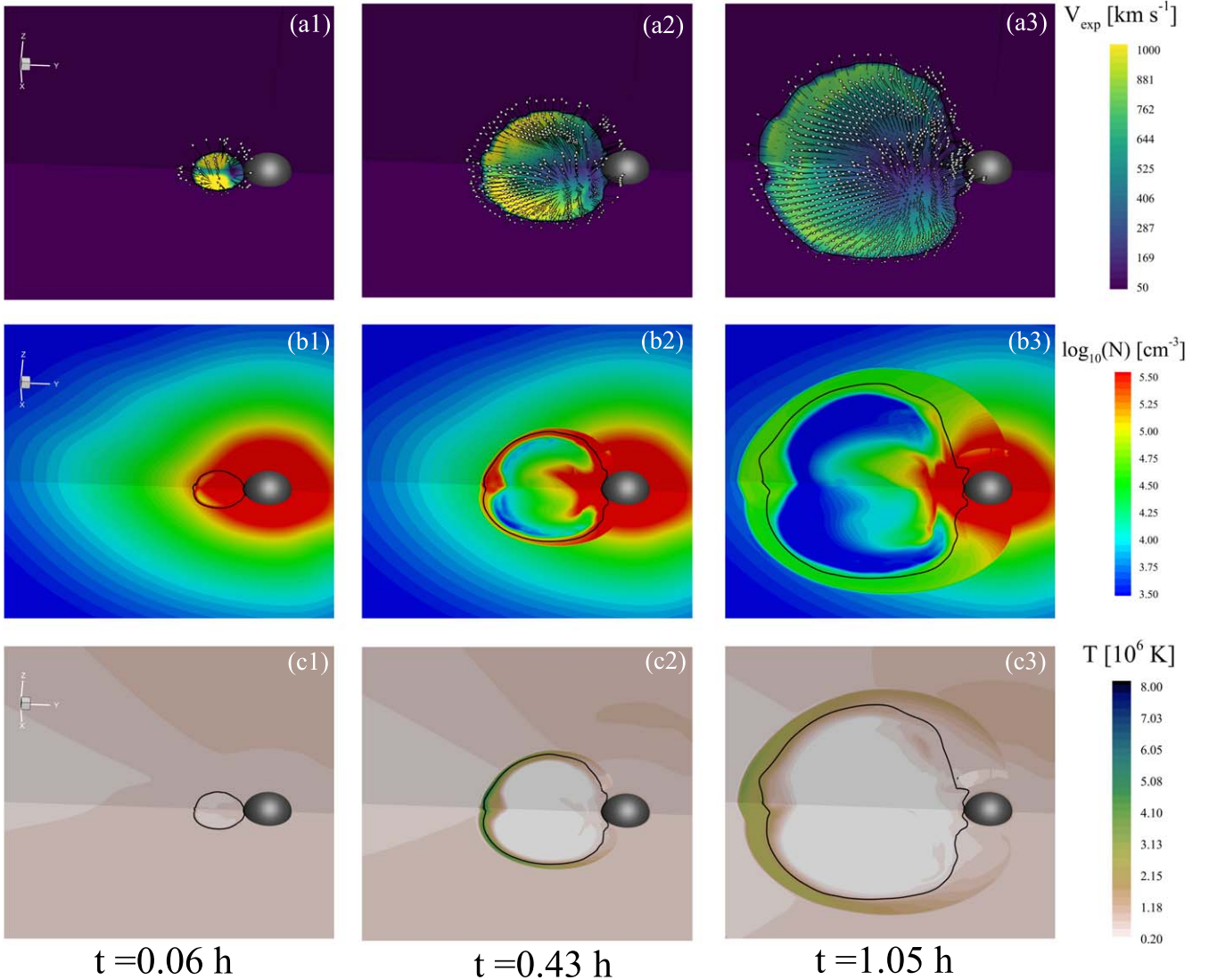
Figure 4. Simulated distributions of the expansion speed V_{exp}, the number density N, and the temperature T on the y–z and x–y planes at $t = 0.06$, 0.43, and 1.05 hr. The arrow indicates the direction of the expansion speed, the black line marks the contour line of $\rho_c = 0.01$, and the black sphere represents the Sun.

different moments, which showcase in detail how the expansion of the CME induces the three-part density structure. At $t = 0.06$ hr, the CME with the nearly uniform density and temperature starts to move out. The strong expansion takes place at the forepart of the CME. At $t = 0.43$ hr, the CME becomes significantly large, and the expansion speed evolves into an uneven distribution in the body of the CME. Evidently, as a result of an overpressure in the CME as compared to the ambient solar wind (C. Scolini et al. 2019), the strong expansion occurs at the outlying area of the CME, where the low-density cavity starts to pop out at this moment. Meanwhile, the expanding CME acts as an extended obstacle against which the solar wind plasma is piled up, and the plasma at the utmost boundary of the CME is compressed. As a result, the high-density front of the CME forms. At $t = 1.05$ hr, the expansion speed within the body of the CME no longer exhibits significant qualitative variations. The high-density front widens, the low-density cavity takes on a complete shape, and the high-density core becomes identifiable. The three-part density structure of the CME develops fully.

In the characteristic three-part structure of CMEs, the bright core of CMEs is conventionally regarded as containing the cool ($\sim 10^4$ K) filament material (T. Podladchikova et al. 2024). However, extreme ultraviolet images of CMEs reveal that the temperature of the CME core is typically on the order of a million Kelvin (X. Cheng et al. 2012; I. G. Hannah & E. P. Kontar 2013; J. Sheoran et al. 2023; H. Song et al. 2024). The CME core may be heated through magnetic reconnection during the CME eruption. As the plasma temperature can not be directly derived from white-light coronagraphs, it remains uncertain how the CME's temperature changes from the inner corona to the outer corona, even though the Ultraviolet Coronagraph Spectrometer on board SOHO has assisted us in understanding the evolution of CME plasma parameters such as the density and temperature (E. Landi et al. 2010). In this context, due to the expansion cooling and no extra heating, the temperature of the CME core decreases from about 10^6 K at $2\,Rs$ to about 10^5 K at $5\,Rs$. The CME temperature does not exhibit a distinct structure and shows low variability within the body of the CME. These temperature characteristics are presented merely to highlight their contrast with those of the CME density.

To examine morphological features of the simulated CME that can be viewed in coronagraph images, we compute the white-light intensity under a series of viewpoint orientations, which are displayed in Figure 5. Here, the top, middle, and bottom in the row of panels represent a vantage point from the ecliptic plane, the middle latitude, and the north solar pole. In the first column of Figure 5, the first and second panels show the CME viewed from the side for a limb event, while the third panel is from the front and represents a halo eruption. We also show the flux rope structure of the CME, which is drawn out by the transparent colored lines in Figure 5. All three figures in the polar view column look similar. At very high latitudes, as observers at different longitudes perceive nearly identical sky planes, the figures in the polar view column look similar.

In the synthetic white-light images at the different perspectives, we find that the CME exhibits the clear three-part morphology when its high-density core lies close enough to the sky plane. In the first row of Figure 5, the views at the Carrington longitude $\phi = 0°$ observe the CME from the side, and with the sky planes passing through the center of the flux rope, a three-part CME is viewed at a vantage point from the ecliptic plane to the middle latitude to the solar pole. In the second row of Figure 5, the flank of the flux rope intersects the sky planes associated with the ecliptic-plane and mid-latitude views at the Carrington longitude $\phi = 315°$, and the CME is featured as a loop event although the perspective is still edge-on. This supports that not all the limb events have all three parts (A. Vourlidas et al. 2013). However, the polar view at the Carrington longitude $\phi = 315°$ shows the clear three-part structure of the CME as the high-density core of the flux rope projects into the sky plane. In the third row of Figure 5, the first and second columns provide a frontal view of the CME, and as a visualized coronagraph rises from the low latitude to the middle latitude, the CME's morphology turns from a halo shape to a loop one. The view at the polar region helps to identify if a halo CME actually has a three-part structure.

4. Summary and Discussion

In this work, the high-resolution simulation of the 2021 December 4 CME with the AMR-SIP-CESE solar wind model is conducted to understand how a flux rope without signatures of prominence evolves into the three-part morphology in the solar corona. The AMR technique of the numerical model allows six levels of grid refinement to clearly capture the CME under this global modeling.

Initially, the density in the CME is set to be uniform, and about half an hour later, the CME displays a high–low–high-density structure, which appears in a coronagraph image as a bright front immediately followed by a dark cavity with a bright core behind. The high-density front overlies the utmost boundary of the CME, and the front materials are composed of the pileup solar wind plasma and the squeezed CME plasma. Both the low-density cavity and the high-density core are located within the CME flux rope structure, with the cavity at the outlying area of the flux rope and the core at its central and rear parts.

The evolution of the CME shows that the expansion of the CME is able to induce the three-part density structure. The moving and bulging CME acts as an extended obstacle against which the solar wind plasma is piled up and meanwhile, the plasma at the utmost boundary of the CME is compressed. These two processes produce the high-density front of the CME. Meanwhile, the strong expansion at the outlying area of the flux rope is generated by the large Lorentz force therein. As the plasma is frozen with the magnetic fields, the strong expansion implies the quick dilution of the plasma. After a while, the low-density cavity is shaped at the outlying area of the flux rope where the strong expansion occurs and the high-density core is reserved in the flux rope's central and rear parts with the weak dilation. The different expansion rates at the different parts of the flux rope lead to distinct rarefaction rates of the plasma, which is the reason why both the low-density cavity and the high-density core form within the flux rope.

It can be seen from Figures 2(c) and (d) that the plasma beta of the CME is lower than 0.01, indicating that the magnetic pressure of the CME dominates over its thermal pressure. Figure 3 demonstrates that the Lorentz force is accountable for the expansion of the CME. Taking these two factors into account, the initial density profile should not exert a substantial influence on the expansion of the CME or on the resulting three-part density structure even when the CME propagates into the higher corona. In fact, we have replaced the constant
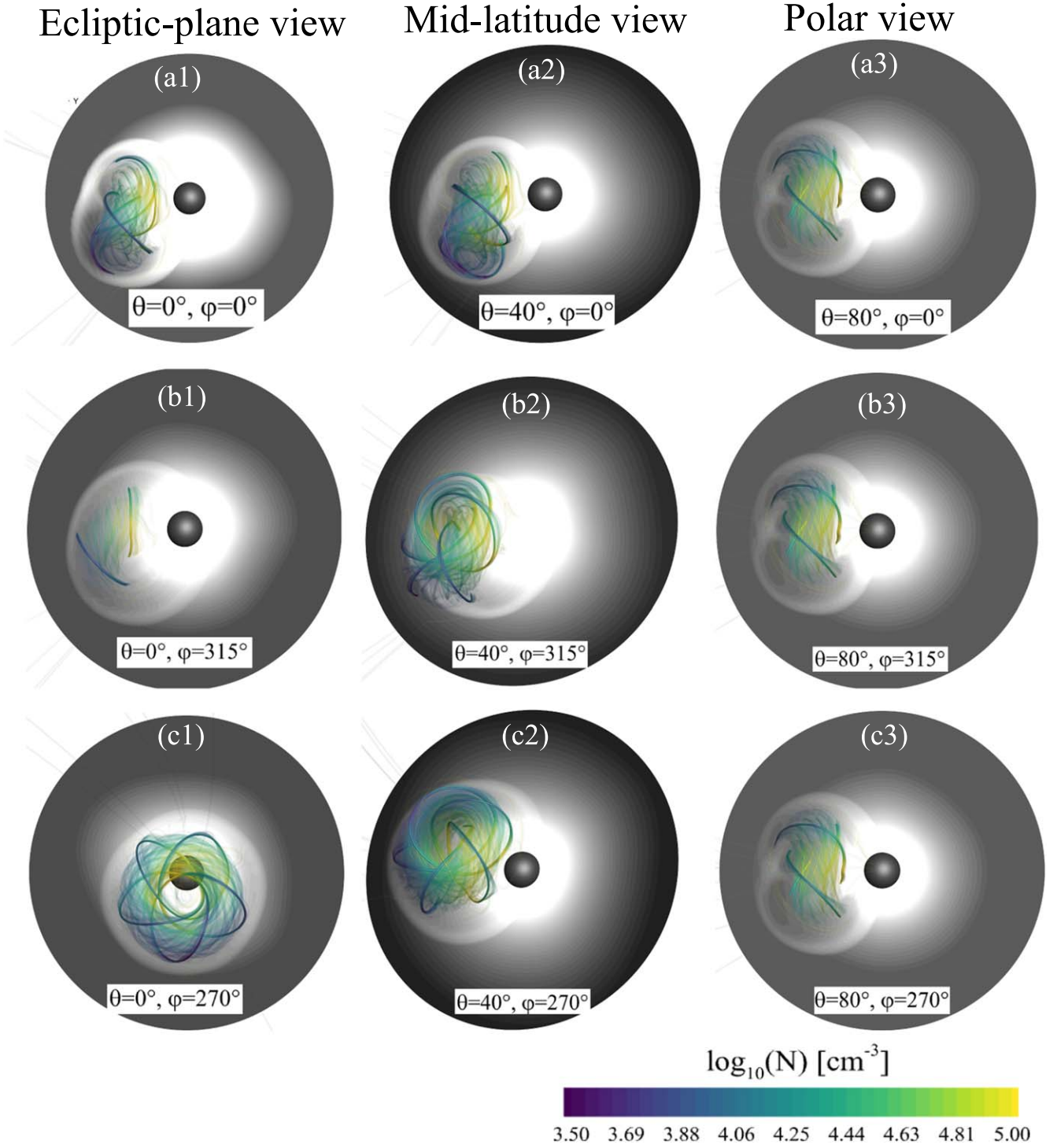
Figure 5. Synthetic images of the white-light intensity as observed from the ecliptic-plane view with the latitude $\theta = 0°$ (left panels), the mid-latitude view with the latitude $\theta = 40°$ (middle panels), and the polar view with the latitude $\theta = 80°$ (right panels), at the Carrington longitude $\phi = 0°$, $\phi = 315°$, and $\phi = 270°$ in the top, middle, and bottom in the column of panels. The transparent colored lines denote magnetic field lines, with the colors representing the number density N.

density profile within the spheromak with the density profile as presented in L. Yang et al. (2021), and the results shown in this paper remain unchanged. Here, we prefer to employ the CME with the initial constant density because our intention was to investigate the net effects of the expansion on the density distribution within the CME, and we do not actually know the exact density profile within CMEs.

Our work demonstrates that the evolution of the flux rope without the dense prominence materials can naturally produce the three-part morphology, and thus explains why some three-part CMEs do not correlate with eruptive prominences. However, it does not rule out the possibility that the high-density core originates from the pre-eruption prominence (G. Zhou et al. 2006; M. Mierla et al. 2023; G. Zimbardo et al. 2023; G. M. Cappello et al. 2024). In our model, the continued expansion of the flux rope makes the high-density core eventually disappear, and the whole flux rope transforms into a tenuous cavity. This conforms to the measurements at far

distances from the Sun that interplanetary flux ropes are low-density (P. Riley et al. 2008; E. Palmerio et al. 2024). Our study also reveals that the temperature of the flux rope is evidently lower than that of the solar wind, and has low variance compared to the density. It is beneficial to use these features of the temperature to identify flux ropes from the solar wind (Y. D. Liu et al. 2024). To observe the three-part morphology, it is disclosed here that favorable projections are necessary. When the high-density core of flux ropes lies close enough to the sky planes, all three parts of the events could be identified in coronagraph images. This may help to understand why only ∼30% of CME events display the three-part morphology (R. A. Howard et al. 2023).

Although observations have indicated that CMEs consist of magnetic flux ropes with foot points remaining anchored to the Sun, their intrinsic magnetic structures are not yet fully resolved (Y. Wang et al. 2009; E. Asvestari et al. 2022). Representing the complex magnetic structure of CMEs with analytical flux rope models is extremely challenging for numerical simulations of CMEs. Here, we use the spheromak flux rope to approximate the magnetic structure of the 2021 December 4 CME as the spheromak flux rope can be prescribed initial parameters commensurate with the observations (G. J. Koehn et al. 2022; L. Yang et al. 2023; R. Sarkar et al. 2024). Unlike the Gibson–Low or Titov–Démoulin flux ropes (N. Lugaz et al. 2005a; L. Linan et al. 2023; M. Zhang et al. 2023), whose foot points remain attached to the Sun, the spheromak flux rope does not support dense prominence plasma, which is suitable for the current study. Due to an overpressure as compared to the background, flux ropes propagating in the solar corona are expected to undergo an uneven expansion and exhibit a density structure. In the future, we plan to integrate into the AMR-SIP-CESE solar wind model the Gibson–Low flux rope (S. E. Gibson & B. C. Low 1998; N. Lugaz et al. 2005b; M. Jin et al. 2017b; E. Provornikova et al. 2024) or a stretching transformation of the spheromak (D. Shiota & R. Kataoka 2016; J. Zhang et al. 2021) to check the global uneven expansion as well as the resulting density structure. Improvements of observational capabilities in current missions (e.g., A. Vourlidas et al. 2016; R. A. Howard et al. 2020; W. Gan et al. 2023) and future missions (e.g., Y. Wang et al. 2020; Y. Deng et al. 2023; N. Gopalswamy et al. 2024) will lead to new insights into the CMEs' morphology, especially the 3D morphology, which will greatly constrain numerical models and make them approach the reality.

ORCID iDs

Liping Yang ⬤ https://orcid.org/0000-0003-4716-2958
Xueshang Feng ⬤ https://orcid.org/0000-0001-8605-2159
Fang Shen ⬤ https://orcid.org/0000-0002-4935-6679
Ming Xiong ⬤ https://orcid.org/0000-0001-9427-7366
Chenglong Shen ⬤ https://orcid.org/0000-0002-3577-5223
Yutian Chi ⬤ https://orcid.org/0000-0001-9315-4487
Yuming Wang ⬤ https://orcid.org/0000-0002-8887-3919
Man Zhang ⬤ https://orcid.org/0000-0003-3000-2819
Xinhua Zhao ⬤ https://orcid.org/0000-0002-9977-2646

References

Asvestari, E., Rindlisbacher, T., Pomoell, J., & Kilpua, E. K. J. 2022, ApJ, 926, 87
Cappello, G. M., Temmer, M., Vourlidas, A., et al. 2024, A&A, 688, A162
Chen, J., Howard, R. A., Brueckner, G. E., et al. 1997, ApJL, 490, L191
Chen, P. F. 2011, LRSP, 8, 1
Cheng, X., Zhang, J., Liu, Y., & Ding, M. D. 2011, ApJL, 732, L25
Cheng, X., Zhang, J., Saar, S. H., & Ding, M. D. 2012, ApJ, 761, 62
Chi, Y., Shen, C., Cheng, L., et al. 2023a, ApJS, 267, 3
Chi, Y., Shen, C., Liu, J., et al. 2023b, ApJL, 951, L14
Deng, Y., Zhou, G., & Dai, S. 2023, ChSBu, 68, 298
Dere, K. P., Brueckner, G. E., Howard, R. A., Michels, D. J., & Delaboudiniere, J. P. 1999, ApJ, 516, 465
Feng, X., Yang, L., Xiang, C., et al. 2012, SoPh, 279, 207
Feng, X., Yang, L., Xiang, C., et al. 2010, ApJ, 723, 300
Feng, X., Zhong, D., Xiang, C., & Zhang, Y. 2013, ScChD, 56, 1864
Gan, W., Zhu, C., Deng, Y., et al. 2023, SoPh, 298, 68
Gibson, S. E., Foster, D., Burkepile, J., de Toma, G., & Stanger, A. 2006, ApJ, 641, 590
Gibson, S. E., & Low, B. C. 1998, ApJ, 493, 460
Gopalswamy, N. 2022, Atmos, 13, 1781
Gopalswamy, N., Christe, S., Fung, S. F., & Gong, Q. 2024, JASTP, 254, 106165
Gopalswamy, N., Makela, P., Yashiro, S., & Davila, J. M. 2012, SunGe, 7, 7
Gopalswamy, N., Mikić, Z., Maia, D., et al. 2006, SSRv, 123, 303
Hannah, I. G., & Kontar, E. P. 2013, A&A, 553, A10
Hildner, E., Gosling, J. T., Hansen, R. T., & Bohlin, J. D. 1975, SoPh, 45, 363
Howard, R. A., Michels, D. J., Sheeley, N. R. J., & Koomen, M. J. 1982, ApJL, 263, L101
Howard, R. A., Sheeley, N. R. J., Michels, D. J., & Koomen, M. J. 1985, JGR, 90, 8173
Howard, R. A., Vourlidas, A., Colaninno, R. C., et al. 2020, A&A, 642, A13
Howard, R. A., Vourlidas, A., & Stenborg, G. 2023, FrASS, 10, 1264226
Howard, T. A., DeForest, C. E., Schneck, U. G., & Alden, C. R. 2017, ApJ, 834, 86
Illing, R. M. E., & Hundhausen, A. J. 1985, JGR, 90, 275
Jiang, C., Feng, X., Liu, R., et al. 2021, NatAs, 5, 1126
Jin, M., Manchester, W. B., van der Holst, B., et al. 2017a, ApJ, 834, 172
Jin, M., Manchester, W. B., van der Holst, B., et al. 2017b, ApJ, 834, 173
Kataoka, R., Ebisuzaki, T., Kusano, K., et al. 2009, JGR, 114, A10102
Koehn, G. J., Desai, R. T., Davies, E. E., et al. 2022, ApJ, 941, 139
Landi, E., Raymond, J. C., Miralles, M. P., & Hara, H. 2010, ApJ, 711, 75
Li, L., Song, H., Peter, H., et al. 2024, ApJ, 967, 130
Linan, L., Regnault, F., Perri, B., et al. 2023, A&A, 675, A101
Liu, Y. D., Hu, H., Zhao, X., Chen, C., & Wang, R. 2024, ApJL, 974, L8
Low, B. C. 1994, PhPl, 1, 1684
Lugaz, N., Manchester, W. B. I., & Gombosi, T. I. 2005a, ApJ, 627, 1019
Lugaz, N., Manchester, W. B. I., & Gombosi, T. I. 2005b, ApJ, 634, 651
Ma, M., Yang, L., Shen, F., et al. 2024, ApJ, 976, 183
Manchester, W., Kilpua, E. K. J., Liu, Y. D., et al. 2017, SSRv, 212, 1159
Manchester, W. B., Gombosi, T. I., Roussev, I., et al. 2004, JGR, 109, A02107
Mei, Z., Ye, J., Li, Y., et al. 2023, ApJ, 958, 15
Mei, Z. X., Keppens, R., Cai, Q. W., et al. 2020, ApJL, 898, L21
Mierla, M., Cremades, H., Andretta, V., et al. 2023, SoPh, 298, 42
Möstl, C., Farrugia, C. J., Temmer, M., et al. 2009, ApJL, 705, L180
Munro, R. H., Gosling, J. T., Hildner, E., et al. 1979, SoPh, 61, 201
Palmerio, E., Carcaboso, F., Khoo, L. Y., et al. 2024, ApJ, 963, 108
Palmerio, E., Maharana, A., Lynch, B. J., et al. 2023, ApJ, 958, 91
Parker, E. N. 1963, Interplanetary Dynamical Processes (New York: Interscience)
Patsourakos, S., Vourlidas, A., & Kliem, B. 2010, A&A, 522, A100
Podladchikova, T., Jain, S., Veronig, A. M., et al. 2024, A&A, 691, A344
Provornikova, E., Merkin, V. G., Vourlidas, A., et al. 2024, ApJ, 977, 106
Riley, P., Lionello, R., Mikić, Z., & Linker, J. 2008, ApJ, 672, 1221
Rouillard, A. P., Davies, J. A., Forsyth, R. J., et al. 2009, JGRA, 114, A07106
Sarkar, R., Pomoell, J., Kilpua, E., et al. 2024, ApJS, 270, 18
Schwenn, R., dal Lago, A., Huttunen, E., & Gonzalez, W. D. 2005, AnGeo, 23, 1033

Schwenn, R., Rosenbauer, H., & Muehlhaeuser, K. H. 1980, GeoRL, 7, 201
Scolini, C., & Palmerio, E. 2024, JSWSC, 14, 13
Scolini, C., Rodriguez, L., Mierla, M., Pomoell, J., & Poedts, S. 2019, A&A, 626, A122
Shen, C., Chi, Y., Wang, Y., Xu, M., & Wang, S. 2017, JGRA, 122, 5931
Sheoran, J., Pant, V., Patel, R., & Banerjee, D. 2023, FrASS, 10, 27
Shiota, D., & Kataoka, R. 2016, SpWea, 14, 56
Song, H., Li, L., & Chen, Y. 2022, ApJ, 933, 68
Song, H., Li, L., Wang, B., Xia, L., & Chen, Y. 2024, ApJ, 978, 40
Song, H., Li, L., Zhou, Z., et al. 2023a, ApJL, 952, L22
Song, H., Zhang, J., Li, L., et al. 2023b, ApJ, 942, 19
Song, H. Q., Cheng, X., Chen, Y., et al. 2017, ApJ, 848, 21
Song, H. Q., Zhang, J., Cheng, X., et al. 2019, ApJ, 883, 43
Thernisien, A. F. R., Howard, R. A., & Vourlidas, A. 2006, ApJ, 652, 763
Veronig, A. M., Podladchikova, T., Dissauer, K., et al. 2018, ApJ, 868, 107
Vourlidas, A., Howard, R. A., Plunkett, S. P., et al. 2016, SSRv, 204, 83
Vourlidas, A., Lynch, B. J., Howard, R. A., & Li, Y. 2013, SoPh, 284, 179
Wang, B. T., Cheng, X., Song, H. Q., & Ding, M. D. 2022, A&A, 666, A166
Wang, Y., Ji, H., Wang, Y., et al. 2020, ScChE, 63, 1699
Wang, Y., Zhang, J., & Shen, C. 2009, JGRA, 114, A10104
Webb, D. F., & Hundhausen, A. J. 1987, SoPh, 108, 383
Wood, B. E., & Howard, R. A. 2009, ApJ, 702, 901
Wood, B. E., Howard, R. A., & Linton, M. G. 2016, ApJ, 816, 67
Wyper, P. F., Lynch, B. J., DeVore, C. R., et al. 2024, ApJ, 975, 168
Xiong, M., Davies, J. A., Bisi, M. M., et al. 2013, SoPh, 285, 369
Yang, L., Hou, C., Feng, X., et al. 2023, ApJ, 942, 65
Yang, L., Wang, H., Feng, X., et al. 2021, ApJ, 918, 31
Yang, L. P., Feng, X. S., Xiang, C. Q., et al. 2012, JGRA, 117, A08110
Yao, S., Marsch, E., Tu, C.-Y., & Schwenn, R. 2010, JGRA, 115, A05103
Yashiro, S., Gopalswamy, N., Michalek, G., et al. 2004, JGRA, 109, A07105
Zhang, J., Temmer, M., Gopalswamy, N., et al. 2021, PEPS, 8, 56
Zhang, M., Feng, X., Li, H., et al. 2023, FrASS, 10, 1105797
Zhang, M., Feng, X. S., & Yang, L. P. 2019, JSWSC, 9, A33
Zhou, G., Wang, Y., & Wang, J. 2006, AdSpR, 38, 466
Zhou, Y., Feng, X., & Zhao, X. 2014, JGRA, 119, 9321
Zimbardo, G., Ying, B., Nisticò, G., et al. 2023, A&A, 676, A48